Numerical Study of Transonic Cavity Flows Using Large-Eddy and Detached-Eddy Simulation

P. Nayyar, D. Lawrie, G. N. Barakos, K. J. Badcock and B. E. Richards

CFD Laboratory, Deparment of Aerospace Engineering,
University of Glasgow, Glasgow, G12 8QQ
http://www.aero.gla.ac.uk/Research/CFD/projects/cavity/cavityflows.htm

Abstract

Numerical simulations of the flow inside a cavity with a length-to-depth ratio (L/D) of 5 and a width-to-depth ratio (W/D) of 1 have been conducted using Large-Eddy Simulation (LES) and Detached-Eddy Simulation (DES). The cavity is exposed to a free-stream of zero incidence, $M_\infty = 0.85$ and $Re = 1 \times 10^6$ (based on the cavity length). Previous numerical simulations of 3D cavities using Unsteady Reynolds-Averaged Navier-Stokes (URANS) have proved difficult in accurately predicting the noise level and frequency content (and hence flow features) inside cavities. Simulation techniques such as LES and DES are therefore applied to the 3D cavity and this paper demonstrates its superior effectiveness relative to URANS in the analysis of cavity flows. Plots depicting the level of noise, frequency content and velocity profiles inside the cavity are presented. Comparisons are made with experimental unsteady pressure and PIV measurements. It was found that both DES and LES fare much better than URANS in resolving the higher frequencies and in predicting the velocity characteristics inside the cavity.

Nomenclature

D	Cavity depth
L	Cavity length
M	Mach number
Re	Reynolds number, $R_e = \frac{\rho u l}{\mu}$
CFD	Computational Fluid Dynamics
PIV	Particle Image Velocimetry
PMB	Parallel MultiBlock - flow solver
URANS	Unsteady Reynolds-Averaged Navier Stokes
SST	Menter's Shear-Stress Transport Model
DES	Detached Eddy Simulation
DNS	Direct Numerical Simulation
LNS	Limited Numerical Scales
LES	Large Eddy Simulation
SGS	Sub-Grid Scale Model
P_{ref}	Pressure reference to audible sound, $P_{ref} = 2\text{x}10^5\text{Pa}$
P_{rms}	Root mean square pressure, $P_{rms} = \sqrt{\frac{(\sum P - P_{mean})^2}{N}}$
SPL	Sound Pressure Level, $SPL = 20log_{10}\left(\frac{Prms}{Pref}\right)$
PSD	Power Spectral Density
C_{w1},f_{w1}	DES constants
$\tilde{d}$,d	Distance to nearest wall
C_{DES}	DES constant
Δ	Metric grid size
l	Turbulent length scale
k	Turbulent kinetic energy
ω	Turbulent dissipation rate specific to turbulent kinetic energy

Introduction

Since the implementation of internal carriage of stores, the cavity flow problem has been widely studied. Interest in this phenomenon lay not only in understanding the complex flow physics but also in alleviating the serious problems that it posed. A highly unsteady flowfield develops inside the cavity with strong vortical interactions with the cavity walls and the shear layer, which covers most of the cavity span and length. An intricate structure of self-sustained pressure oscillations instigate buffetting and produce a harsh acoustic environment within the cavity. The noise level can be found to approach 170 dB and has serious connotations on the structural integrity of equipment (e.g. stores, avionics etc.) housed within and around the cavity. Longer (and shallower) cavities are also known to experience large pitching moments that can have adverse effects on the release characteristics of stores.

Numerous experimental investigations have been performed on cavity flows in an attempt to better understand the problem. Ross *et al.* from QinetiQ[1–3] conducted a significant number of wind tunnel experiments on cavities of several configurations over a broad range of Mach and Reynolds numbers and also provided experimental data on cavity acoustical suppression methods which employ leading-edge spoilers and vortex-shedding rods amongst others. Recent experiments have exploited advanced non-intrusive, optical techniques such as Particle Image Velocimetry (PIV)[4, 5] and Laser Doppler Velocimetry (LDV)[6] for high-fidelity, high-resolution data acquisition about the instantaneous flow-field and velocity variations inside the cavity. Such methods are however expensive and are either restricted to low Reynolds number flow visualisation or are not sufficiently accurate for highly time-dependent flows. For cavity flows, which are intrinsically unsteady, experimental techniques such as PIV still require further development[4].

Recent studies of cavity flows have therefore attempted to use Computational Fluid Dynamics (CFD) as an analysis tool, with most emphasis on the use of Reynolds-Averaged Navier-Stokes (RANS) equations in conjunction with various turbulence models to resolve the flow characteristics[7–10]. In high Reynolds flows, however, a broad range of turbulent length and time scales persist. For the cavity, this intense turbulent environment is further coupled with strong acoustic radiations, the source of which is located at the downstream edge of the cavity. The acoustical signature in the cavity is composed of broadband noise (lower-frequency, lower-energy noise contributed by the freestream and/or the shear layer) with the narrowband noise (a combination of higher-frequency and lower-frequency noise of different magnitude contributed by vortex-vortex, vortex-wall, vortex-shear layer, shock-shear layer and shear layer-wall interactions) superimposed on it. The narrowband spectrum comprises of discrete acoustic tones that are eponymously referred to as Rossiter modes after J. E. Rossiter who developed a semi-empirical formula to calculate them[11]. Statistical turbulence models tend to predict the larger, more energetic scales (associated with the lower-frequency discrete acoustic tones) well but fail to provide the same accuracy in capturing the smaller, higher-frequency and more intermittent time scales. The broadband noise is also not captured at all by these models.

The strive for better resolution of the turbulent flowfield and the acoustical signature of cavity flows has recently led to attention being diverted from the use of purely statistical models in the application of cavity flows towards simulation methods such as Large-Eddy Simulation (LES). LES puts less emphasis on modelling the flow properties and in-

stead works by filtering the flow structures in terms of their scale size. The larger scales, which are dictated by geometry and boundary conditions, are explicitly resolved whereas the smaller scales, which are less influenced by the geometry and tend to be more isotropic, are modelled using a sub-grid scale (SGS) model. Rizzetta[12] from the Air Force Research Laboratory, Smith[13] from Lockheed Martin and Larcheveque *et al.* [14] have all successfully applied LES to cavity flows.

LES is however not bereft of problems. It has difficulty in resolving the turbulent stresses in the near-wall region where the required resources approach DNS. And with pure LES offering flows with Reynolds number only 10 times higher than what can be tackled with DNS with the current computational resources, recent endeavours have further looked at developing hybrids of RANS and LES to compromise the best of both methods. The Detached-Eddy Simulation (DES) method proposed by Spalart[15] is one such example and involves modifying the one-equation Spalart-Allmaras turbulence model so that RANS is activated in the near-wall and boundary layer regions and LES elsewhere. For closures other than the Spalart-Allmaras (e.g. for two- equation turbulence models), a similar idea was initially put forward by Strelets[16] and Batten and Goldberg[17] (the latter calling their method Limited Numerical Scales (LNS)). Shieh and Morris [18] and Vishwanathan and Squires[19] also discuss results with DES-like approaches to cavity flows with a good degree of success.

The objective of the present work is to perform LES and DES for a transonic flow over a clean, rectangular, open cavity for both the no-doors and doors-on (at 90^o) configurations (Figures 1 and 2(a)). The small-scale turbulent structures are realised with the classical Smagorinsky SGS for LES computations whereas the one-equation Spalart-Allmaras model was used to resolve near-wall features for the DES method. The cavity geometry is pictorially depicted in Figure 1. The cavity has a length-to-depth ratio (L/D) of 5 and a width-to-depth ratio (W/D) of 1. The free-stream Mach and Reynolds number (based on the cavity length) are 0.85 and 1 million, respectively. Pressure values from computations were compared with experimental pressure measurements at the locations specified in Figure 1. This paper also endeavours to provide a better understanding of the turbulent flow-field inside the cavity by presenting comparisons of velocity profiles with PIV measurements.

Mathematical Model

CFD Solver

All computations were performed using the Parallel Multi-Block (PMB) flow solver[20] developed at the University of Glasgow, which has been continually revised and updated over a number of years. LES and DES formulations were originally implemented into the code for this project[21] and have since then been used for other applications. At the moment, the classical Smagorinsky SGS is used for LES whereas DES with both the one-equation Spalart-Allmaras and the two-equation $k-\omega$ and SST turbulence models have been integrated. The solver has been successfully applied to a variety of problems including cavity flows, hypersonic film cooling, spiked bodies, flutter and delta wing flows amongst others.

The code solves the unsteady Reynolds Averaged Navier Stokes equations on multiblock structured grids, in serial or parallel mode. Governing equations are discretised using a cell-centered finite volume method. The convective terms are discretised using either Osher's or Roe's scheme. MUSCL interpolation is used to provide nominally third order ac-

curacy and the Van Albada limiter is used to avoid spurious oscillations across shocks. The time-marching of the solution is based on an implicit, dual time stepping method. The final algebraic system of equations is solved using a Conjugate Gradient method, in conjunction with Block Incomplete Lower Upper factorisation. A number of turbulence models have been implemented[21].

DES Formulation

Spalart[15] modified the one-equation Spalart-Allmaras model to achieve a DES equivalent. The only modification is in the dissipation term of the transport equation of $\tilde{\nu}$:

$$-C_{w1} f_{w1} \left(\frac{\tilde{\nu}}{\tilde{d}}\right)^2 \tag{1}$$

Originally,

$$\tilde{d} = d = \text{distance of the nearest wall} \tag{2}$$

whereas for DES, it is:

$$\tilde{d} = C_{DES}\Delta \tag{3}$$

where C_{DES} is the DES coefficient and
Δ is the metric of the grid size.

In practice, the following is employed although other metric relations are also possible:

$$\tilde{d} = \min\left(d, C_{DES}\Delta\right) \tag{4}$$

$$\Delta = \max\left(\Delta_x, \Delta_y, \Delta_z\right) \quad \forall \quad \text{cell.} \tag{5}$$

The concept of employing a DES-like approach for turbulence models other than the one-equation Spalart-Allmaras was originally proposed by Strelets[16] and later by Batten and Goldberg[17]. For the two-equation $k-\omega$ model, for instance, the only modification, as with the one-equation Spalart-Allmaras DES variant, is in the dissipation term:

$$-\beta^* \rho \omega k \tag{6}$$

The turbulent length scale is defined by:

$$l = \frac{k^{1/2}}{\beta^* \omega} \tag{7}$$

Re-arranging for $\beta^*\omega$ and substituting into equation 6 gives:

$$-\rho \frac{k^{3/2}}{l} \tag{8}$$

where l is given by:

$$l = \min\left(l, C_{DES}\Delta\right) \tag{9}$$

C_{DES} is set to 0.78 and Δ is as before.

Description of Wind Tunnel & PIV Experiments

Wind tunnel experiments conducted by Ross[3] at Aircraft Research Association Ltd (ARA) at Bedford, UK, were used for CFD comparisons. The ARA wind tunnel is a 9 by 8 foot continuous flow, transonic wind tunnel (TWT) with ventilated roof, floor and side walls.

The L/D=5 cavity model (with W/D=1) measured 20 inches in length and 4 inches in width and depth. In the doors-on configuration, the doors were positioned at the front and rear walls in the z-direction and spanned the entire length of the cavity (see Figure 2(a)) and measured 0.375 in width and 2 inches in height. The generic cavity rig model (designated as Model M219) was positioned at zero incidence and sideslip and the wind tunnel was operated at a Mach number of 0.85 and atmospheric pressure and temperature. Unsteady pressure measurements were registered inside and outside the cavity via Kulite pressure transducers: 10 pressure transducers were aligned along the centerline of the floor of the cavity rig (shown in Figure 1, 2 on the flat plate ahead of the cavity, 1 on the flat plate aft of the cavity, 2 on the front and rear walls and 4 on the port

side walls[3]. The data was sampled at 6000 Hz using a high-speed digital data acquisition system.

The measured data was presented in terms of Sound Pressure Level (SPL) and Power Spectral Density (PSD) plots. The SPLs are an indication of the intensity of noise generated inside the cavity and can be obtained from the measurements using the following equation:

$$\mathrm{SPL\,(dB)} = 20\log_{10}\left(\frac{\mathrm{P_{rms}}}{2\times10^{-5}}\right) \qquad (10)$$

where the P_{rms} is the RMS pressure normalised by the International Standard for the minimum audible sound of 2×10^{-5} Pa. Spectral analysis was performed using Fast Fourier Transform (FFT) to obtain the power spectral density, which presents the RMS pressure versus frequency and is a measure of the frequency content inside the cavity.

Measurements of the cavity flowfield were provided by PIV experiments conducted by Ross[4]. A stereoscopic two-camera system was employed for velocity measurements accompanied with a two-head Nd-YaG laser. Each laser pulse was fired within time intervals of 1μs. Four data acquisitions were taken with each acquisition comprising of 2 photographic images taken at 1μs intervals. The width of the laser sheet was limited to approximately 5.5 inches so the total cavity length of 20 inches was captured in 4 sections using motorised camera/laser traverse gear (Figure 2(b)). Seeding was provided by various combinations of water droplets sprayed in the settling chamber and vegetable oil mist diffusion from small holes in the cavity floor. Analysis of the data signals was performed by phase-locking onto each peak of signal and introducing a series of delays to synchronise image acquisitions at a particular part of the cycle. A number of acquisitions were then taken and averaged to define the flowfield at that part of the cycle. For highly unsteady flows with multiple cyclic components, it was recognised that phase-locking on any one component does not 'freeze' the flowfield. As highlighted by Ross[4], combined with the highly turbulent background, all aspects of cavity flow are not likely to be accounted for. For complete definition of the flowfield with time-dependency, very high-speed image acquisition equipment would be required.

Results & Discussion

Comparisons between the URANS, LES and DES for the cavity with and without doors are depicted in plots from Figures 3 to 7. The grids used for these calculations are detailed in Table 1. Where flows of Reynolds number of the order of millions are concerned, as is the case here, 2.2 million points for a grid for LES calculations, in particular, is evidently not sufficient. Calculations on higher resolution grids are currently under way but could not be analysed in time for this paper.

Figure 3 shows the difference between the LES and URANS methods in the prediction of noise levels and frequencies for the clean, doors-on cavity configuration. Both methods agree well with experiment. In fact, near the rear of the cavity, the shape of the SPL curve for the baseline SST model follows the experiment better than the LES counterpart. Frequency content analysis is made via spectral plots (Figure 3(b)) and this illustrates a less promising agreement between the baseline SST model and experiment. Neither the 1st nor the 3rd Rossiter modes were captured - refer to Table 2 for quantitative comparison between the frequencies and amplitudes predicted between the computations and experiment. The 2nd Rossiter mode ($\approx$ 400 Hz) is well captured but is over-predicted by about 1 kPa. This over-prediction was found to be a common occurrence for most URANS comparisons with

experiment. LES, however, generally provides better agreement with all the 4 discrete acoustic tones in terms of their phase and amplitude, except for the 2nd Rossiter mode which is slightly under-predicted. Analysis of the windowed SPL plots in Figure 4, which scrutinises the fluctuation in noise level along the cavity floor for each of the 4 Rossiter modes that are predominantly found in cavity flows at this transonic flow regime, supports this. The best agreement for the baseline SST model with experiment exists only for the 2nd Rossiter mode ($\approx$ 400 Hz): both the shape and amplitude are better predicted than the current LES on a coarse grid of 2.2 million points. Since this 2nd Rossiter mode is the dominant mode as is justified by the relative values of SPL in Figure 4, the URANS results look good at a first glance. Inspection of the other 3 modes, reveals that a significantly better comparison exists between LES and experiment. In general, LES captures the higher frequencies much better than URANS.

Results from the clean, no-doors cavity for the URANS, DES and LES methods are depicted in Figures 5 to 7, with unsteady pressure comparisons with experiment revealing best agreement with DES and LES. The shape of the SPL curve for the baseline SST model still resembles the 'W' shape that is characteristic of the doors-on case Figure 3(a). The major difference the absence of doors has on the flow is the greater transport and/or redistribution of momentum in the spanwise direction for the clean cavity case. The fact that the baseline SST model predicts a completely incorrect SPL shape (unlike the LES and DES) suggests that the baseline SST model (and indeed URANS) has difficulty in accommodating effects of the spanwise dimension and indeed the stronger transport and diffusion of energy and momentum in this direction. The difference in frequencies without the doors is clearly represented by the spectral analysis in Figure 5(b). The 3rd Rossiter mode is more dominant for the no-doors cavity case compared to the 2nd mode for the doors-on case and suggests that the 3rd mode is correlated to the presence of the z-dimension and/or the transport/redistribution of energy into this direction. Although the baseline SST model predicts the 3rd mode relatively well it fails to account for any of either the lower or higher frequencies. Closer inspection by the windowed SPL plots in Figure 6 further emphasises the better agreement between experiment and the simulation techniques rather than URANS.

Instantaneous flowfield plots of Mach contours for both the baseline SST model and DES (with the one-equation Spalart-Allmaras model) along the cavity centerline are illustrated in Figure 7. The Mach number plots distinctly demarcates the lower-velocity regions (blue) inside the cavity from the transonic regions (yellow) outside the cavity. Where these two regions coincide is where the shear layer is located. The baseline SST model always predicts a larger single primary vortex structure at the cavity rear with some combination of two or more counter-rotating vortices at the cavity front. The shear layer is also consistently found to span the cavity with distinct deflection at the cavity rear (Figure 7). It is this dual-vortex cycle inside the cavity that results in the 'W'-shaped SPL curve in Figure 5(a). The DES, however, portrays a different picture and is something that is perhaps more intuitively correct for the clean, no-doors cavity. One crucial difference between the DES and URANS flowfield results lies in the behaviour of the shear layer and this is evident in Figure 7. At no point for the DES computations does the shear layer extend across the entire length of the cavity. At the most, the shear layer can be observed to be coherent up to the middle of the cavity at which point, if not earlier, it breaks down. What follows is intensive mixing and spreading of the energy

from the shear layer and the free- stream with the lower-velocity flow region inside the cavity.

Since both the doors-on and clean cases were run at identical flow conditions, the mean flow energy imparted from the free-stream and the turbulent flow energy imparted from the oncoming boundary layer (the height of which is also identical in both cases) is identical. Presence of the doors channels the flow into the cavity and prevents any leakage into the spanwise direction and the flow behaves as if it were two-dimensional. All the energy from the oncoming boundary layer is therefore concentrated into the shear layer, which maintains its flow path in the streamwise and transverse plane. The confining presence of the doors preclude any transfer of energy into the spanwise direction outside the cavity. Even inside the cavity, little transport and/or redistribution of energy towards the width of the cavity occurs and this is indicative of insignificant three-dimensionality effects. For the clean cavity case, however, there is a means for energy to be redistributed into the spanwise direction both outside and consequently inside the cavity. Energy is therefore extracted from the shear layer and spread into the surroundings. The pressure at the cavity rear rises due to this mixing process and is manifested in the form of a rising SPL curve (refer to Figure 5(a)). Some evidence of this breakdown of the shear layer for the clean cavity with no-doors is also evident from the PIV experiment in Figure 8 which depicts a snapshot of the flowfield inside the cavity using velocity magnitude contours and streamlines. The shear layer can clearly be observed to extend to approximately the middle of the cavity beyond which it breaks down. The change in direction of the streamlines at the cavity rear is indicative of the redistribution of energy and momentum from the shear layer into the cavity. This breakdown of the shear layer is, however, not observed at all in the baseline model (Figure 7) and is probably why the baseline model and indeed URANS fail to correctly predict the noise level and frequencies inside the cavity.

Streamwise and transverse velocity profiles for three different stations inside the cavity (x/L=0.05, x/L=0.55 and x/L=0.95 - see Figure 1 for reference to positions of these pressure taps) for both DES and LES are illustrated in Figures 9 and 10, respectively. Results are compared with the PIV measurements, details of which were provided earlier, supplied by Ross[4]. In the figures, the black line is denoted as the PIV data. Four other plots are included in each velocity profile plot and these correspond to the time-averaged DES results for the coarse and fine grids (refer to Table 1 for information on the grids used) at CFD time-steps of 0.01 ($\equiv 1.814 \times 10^{-5}$s) and 0.005 ($\equiv 9.07 \times 10^{-6}$s) in Figure 9 and their LES equivalent in Figure 10. The results are encouragingly consistent for both DES and LES, with the fine grid with the fine time-step for the most part providing the best agreement.

Agreement with PIV is, however, sensitive to the station analysed. At the first two stations, for instance, i.e. at x/L=0.05 (cavity front) and at x/L=0.55 (cavity middle), the agreement between DES, LES and PIV is good. At the cavity rear (x/L=0.95), agreement with PIV deteriorates. The explanation for this may lie in the manner in which the PIV experiment was conducted. As mentioned previously, the laser used for the PIV experiment had a width of approximately 5.5 inches, which is roughly equivalent to a quarter of the cavity length. The laser was therefore required to be fired at four different sections in order to cover the entire length of the cavity (Figure 2(b)). The resolution of the PIV experiment was found to be good at the first two stations that the computational results were analysed at, i.e. at x/L=0.05 and x/L=0.55, but was not at the third station, i.e. at x/L=0.95. This is illustrated in Figure 11, which indicates the variations in the streamwise and transverse velocity

components along the length of the cavity for the PIV experiment at a distance equal to the depth of the cavity above the cavity lip. The experiment was conducted at a Mach number of 0.85 and a freestream velocity of 296 m/s. In sections 1 and 3 of the PIV experiment, which is where the first two stations x/L=0.05 and x/L=0.55 lie, the laser resolution is good and the streamwise velocity is close to its anticipated value of 296 m/s (Figure 11(a)). In section 4, however, which is where the third station x/L=0.95 lies, the resolution deteriorates and the streamwise fluctutations are significantly larger. A consistent story is told by the transverse streamwise plots in Figure 11(b). This may be one plausible reason as to why there are discrepancies between the LES, DES and PIV data at the cavity rear. This also further emphasises the problems with using PIV for highly unsteady flows at high Mach and Reynolds numbers. As mentioned by Ross[4], higher imaging and data acquisition equipment is likely to be required for consistently good resolution throughout the cavity cross-section.

Conclusions

Large-Eddy and Detached-Eddy Simulations of a 3D clean cavity with and without doors and a L/D=5 and W/D=1 at a Mach number of 0.85 and a Reynolds number of 1 million (based on the cavity length) were performed with the PMB code developed at the University of Glasgow. Analysis of unsteady pressure measurements with experiment revealed that both DES and LES consistently gave better agreement than URANS in terms of both frequency content and phase and noise levels for both the doors-on and no-doors configurations.

The baseline SST model was also run for this 3D cavity with and without doors but had difficulty in capturing most of the higher (and in some cases, some of the lower) frequencies in both cases. For the no-doors case, the baseline SST model still predicted a 'W'-shaped SPL curve as it did for the doors-on case unlike LES and DES which correctly predicted the 'tick'-shape.

Windowed SPL plots further indicated that both LES and DES fared much better than URANS to predict the shapes of the SPL curves for each of the first four Rossiter modes found in the cavity for this flow regime, with stark differences between URANS, LES and DES discernibly observed at the higher frequency end.

Analysis of flowfield plots for the no-doors cavity with the baseline SST model and DES revealed that DES predicted a breakdown of the shear layer while the baseline SST model consistenly illustrated a coherent shear layer that spanned the cavity. It was concluded that URANS had difficulty in accounting for the larger transport and/or diffusion of energy and momentum present in the no-doors case.

Streamwise and transverse velocity plots were compared with PIV measurements and showed consistently good agreement at the cavity front and middle for various grid sizes and time-steps for both DES and LES computations. At the cavity rear, the agreement with PIV deteriorated and these discrepancies may be attributed to the poor resolution in the PIV experiment at this point.

Grids used for LES, in particular, are however very coarse. Simulations with higher-resolution grids are intended to be run in the near future.

Acknowledgments

The work detailed in this paper was supported by both BAE Systems and Qinetiq. The authors would like to extend their gratitude to Drs. John Ross and Graham Foster of Qine-

tiq (Bedford) for providing the experimental data.

References

[1] J.A. Ross and J.W. Peto. Internal Stores Carriage Research at RAE. Technical Report 2233, Royal Aircraft Establishment, January 1992.

[2] J.A. Ross and J.W. Peto. The Effect of Cavity Shaping, Front Spoilers and Ceiling Bleed on Loads Acting on Stores, and on the Unsteady Environment Within Weapon Bays. Technical report, QinetiQ, March 1997.

[3] J.A. Ross. Cavity Acoustic Measurements at High Speeds. Technical Report DERA/MSS/MSFC2/TR000173, QinetiQ, March 2000.

[4] J.A. Ross. PIV Measurements of the Flowfields in an Aerodynamically Deep Cavity, May 2002. Private Communication.

[5] S.A. Ritchie, N.J. Lawson and K. Knowles. An Experimental and Numerical Investigation of an Open Transonic Cavity. In *21st Applied Aerodynamics Conference*, Orlando, Florida, June 2003. AIAA.

[6] M.J. Esteve, P. Reulet and P. Millan. Flow Field Characterisation within a Rectangular Cavity. In *10th International Symposium Applications of Laser Techniques to Fluid Mechanics*, July 2000.

[7] D.P. Rizzetta. Numerical Simulation of Supersonic Flow Over a Three-Dimensional Cavity. *AIAA*, 26(7):799–807, July 1988.

[8] X. Zhang. Compressible Cavity Flow Oscillation due to Shear Layer Instabilities and Pressure Feedback. *AIAA*, 33(8): 1404–1411, August 1995.

[9] P.D. Orkwis and P.J. Disimile. Transient Shear Layer Dynamics of Two- and Three-Dimensional Open Cavities. Technical Report ADA 298030, Air Force Office of Scientific Research, 1995.

[10] J. Henderson. *Investigation of Cavity Flow Aerodynamics Using Computational Fluid Dynamics*. PhD thesis, University of Glasgow, 2001.

[11] J.E. Rossiter. Wind Tunnel Experiments on the Flow Over Rectangular Cavities at Subsonic and Transonic Speeds. Technical Report 64037, Royal Aircraft Establishment, October 1964.

[12] D.P. Rizzetta and M.R. Visbal. Large-Eddy Simulation of Supersonic Cavity Flowfields Including Flow Control. In *32nd AIAA Fluid Dynamics Conference*. AIAA, 2002. AIAA Paper 2003-0778.

[13] B.R. Smith, T.J. Welterlen and N.D. Domel. Large Eddy-Simulation for the Analysis of Weapon Bays Flows. Technical report, Lockheed Martin Aeronautics Company, June 2001.

[14] L. Larchevêque, P. Sagaut and T-H Lê. Large-Eddy Simulation of Flows in Weapon Bays. In *41st AIAA Aerospace Sciences Meeting and Exhibit*. AIAA, 2003. AIAA Paper 2003-0778.

[15] P.R. Spalart. Strategies for Turbulence Modelling and Simulations. *International Journal of Heat and Fluid Flow*, 21:252–263, February 2000.

[16] M. Strelets. Detached Eddy Simulation of Massively Separated Flows. In *39th AIAA Aerospace Sciences Meeting*. AIAA, January 2001. AIAA Paper 2001-0879.

[17] P. Batten, U. Goldberg and S. Chakravarthy. Sub-Grid Turbulence Modeling for Unsteady Flow with Acoustic Resonance. In *38th AIAA Aerospace Sciences*. AIAA, January 2000. AIAA Paper 00-0473.

[18] C.M. Shieh and P.J. Morris. Comparison of Two- and Three-Dimensional Turbulent Cavity Flows. In *39th AIAA Aerospace Sciences*. AIAA, January 2001. AIAA Paper 2001-0511.

[19] A.K. Vishwanathan and K.D. Squires. Detached Eddy Simulation of the Flow over an Axisymmetric Cavity. In *Aerospace Sciences Meeting 2003*. AIAA, January 2003. AIAA Paper 2003-0265.

[20] K.J. Badcock, B.E. Richards and M.A. Woodgate. Elements of Computational Fluid Dynamics on Block Structured Grids Using Implicit Solvers. *Progress in Aerospace Sciences*, 36: 351–392, 2000.

[21] P. Nayyar and G. Barakos. A Summary of Turbulence Modelling Approaches in CFD. Technical report, University of Glasgow, 2002. Aerospace Engineering Report 0206.

Grid Type	Pts. in Cavity (Overall)	Wall-Spacing	Blocks in cavity (Overall)
Clean cavity with doors-on (at 90^o)			
3D URANS	446,824 (1,483,173)	1×10^{-5}	20 (110)
3D LES/DES (Coarse)	179,520 (1,248,544)	3.125×10^{-3}	64 (240)
3D LES/DES (Medium)	493,679 (2,218,854)	3.125×10^{-3}	64 (240)
3D LES/DES (Fine)	1,177,646 (4,783,162)	7.1825×10^{-4}	64 (240)
Clean cavity with no-doors			
3D URANS	305,424 (1,174,824)	2.214×10^{-5}	20 (110)
3D LES/DES (Coarse)	179,520 (1,225,824)	3.125×10^{-3}	64 (256)
3D LES/DES (Medium)	493,679 (2,178,480)	3.125×10^{-3}	64 (256)
3D LES/DES (Fine)	1,177,646 (4,696,128)	7.1825×10^{-4}	64 (256)

Table 1: Information about the points, blocks and wall-spacing for the 3D grids used for both the clean cavity in the no-doors and the doors-on at 90^o configurations. The same grid is used for both LES and DES calculations and a different one for the URANS method.

Method	1st Mode (Hz (Pa))	2nd Mode (Hz (Pa))	3rd Mode (Hz (Pa))	4th Mode (Hz (Pa))
Rossiter's Formula	162 Hz (- Pa)	378 Hz (- Pa)	594 Hz (- Pa)	811 (- Pa)
Clean cavity with doors-on (at 90^o)				
Experiment	164 Hz (1300 Pa)	379 Hz (4000 Pa)	583 Hz (700 Pa)	836 Hz (600 Pa)
LES	150 Hz (1300 Pa)	410 Hz (2800 Pa)	585 Hz (700 Pa)	820 Hz (400 Pa)
Baseline SST	- Hz (- Pa)	385 Hz (5100 Pa)	- Hz (- Pa)	770 (700 Pa)
Clean Cavity with no-doors				
Experiment	170 Hz (700 Pa)	360 Hz (1450 Pa)	590 Hz (2000 Pa)	790 Hz (350 Pa)
LES	185 Hz (850 Pa)	380 Hz (1200 Pa)	590 Hz (750 Pa)	790 Hz (450 Pa)
DES	195 Hz (950 Pa)	380 Hz (1000 Pa)	600 Hz (2100 Pa)	800 Hz (400 Pa)
Baseline SST	175 Hz (200 Pa)	380 Hz (350 Pa)	590 Hz (1500 Pa)	- Hz (- Pa)

Table 2: Comparisons of (approximate) frequencies and amplitudes predicted between LES, DES and URANS (Baseline SST turbulence model) for both the no-doors and doors-on clean cavity configurations (at the cavity rear i.e. at x/L=0.95) and the semi-empirical Rossiter's formula and experiment. See Figure 1 for reference to positions of pressure taps. See Table 1 for details on grids used. Note that for the Baseline SST case for the doors-on case, only the 2nd and 4th Rossiter modes exist.

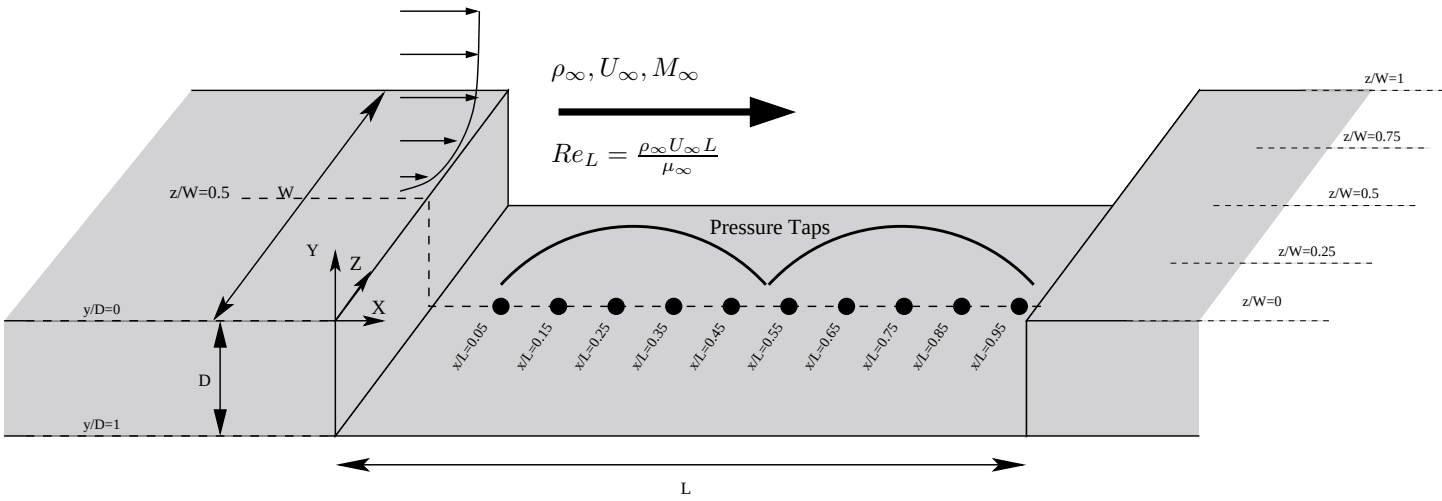

Figure 1: Schematic of cavity geometry and description of notation used when referring to the different positions in the cavity. The 10 pressure taps indicated at the cavity floor (denoted by black dots) correspond to the experimental pressure locations and is where the SPL and PSD data was calculated and compared.

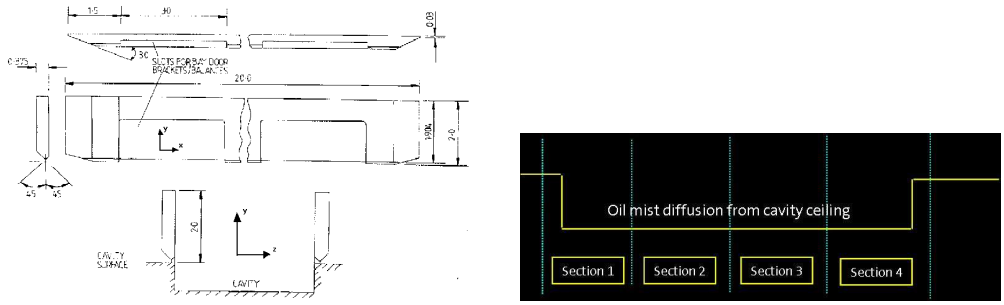

(a) Cavity Geometry with Doors **(b)** PIV Experiment

Figure 2: Schematic of the wind tunnel cavity geometry (including the doors-on configuration) on the left and an illustration of the 4 different sections along cavity for which laser data acquisitions were taken with the PIV experiment on the right.

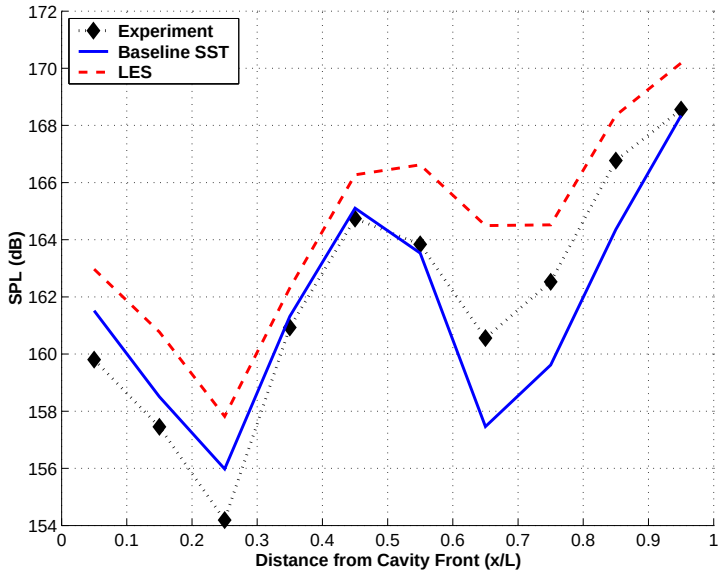

(a) SPL Plots

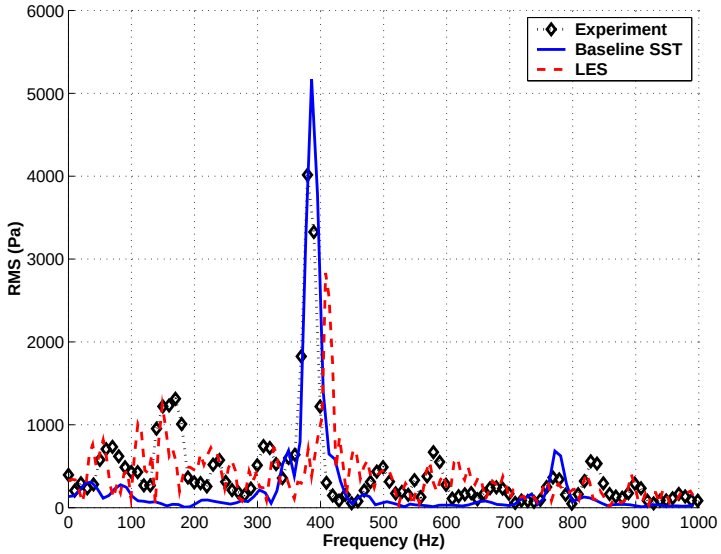

(b) PSD Plots (x/L=0.95)

Figure 3: SPL and PSD plots of L/D=5, W/D=1, clean cavity with doors-on at 90° vertically with URANS (Baseline SST turbulence model) and LES (Smagorinsky SGS) with CFD time-step of 0.01 ($\equiv 1.814 \times 10^{-5}$s). Both plots taken along cavity centreline (z/W=0.5) and at the cavity floor (y/D=1). See Figure 1 for reference to positions of pressure taps and Table 1 for details of the grids employed.

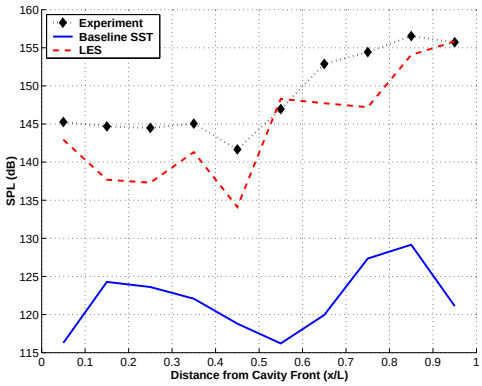

(a) 1st Rossiter Mode (≈ 160 Hz)

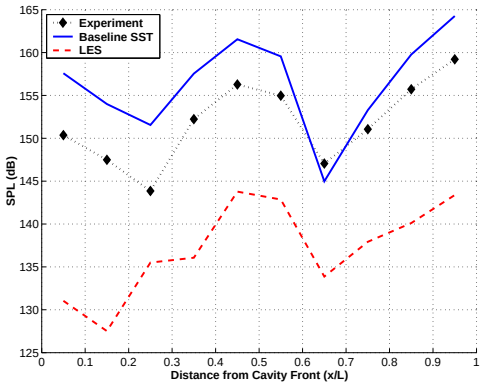

(b) 2nd Rossiter Mode (≈ 380 Hz)

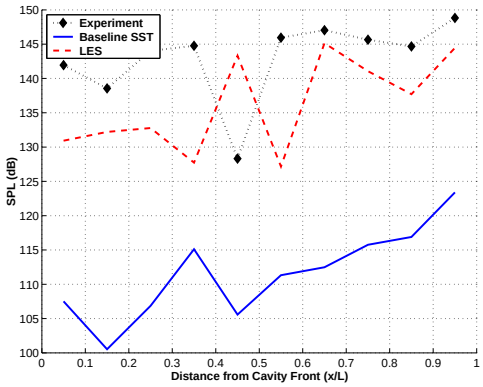

(c) 3rd Rossiter Mode (≈ 600 Hz)

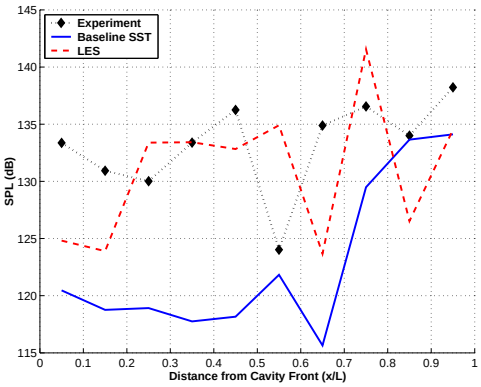

(d) 4th Rossiter Mode (≈ 820 Hz)

Figure 4: Windowed SPL plots of L/D=5, W/D=1 for the clean cavity with doors-on at 90^o vertically with URANS (Baseline SST turbulence model) and LES (Smagorinsky SGS) compared with experiment for the first 4 Rossiter modes. Plots taken along cavity centreline (z/W=0.5) and at the cavity floor (y/D=1). See Figure 1 for reference to positions of pressure taps and Table 1 for details of the grids employed.

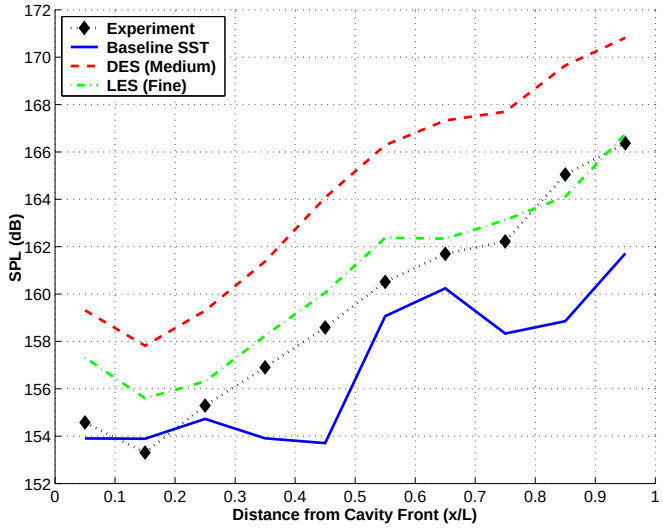

(a) SPL Plots

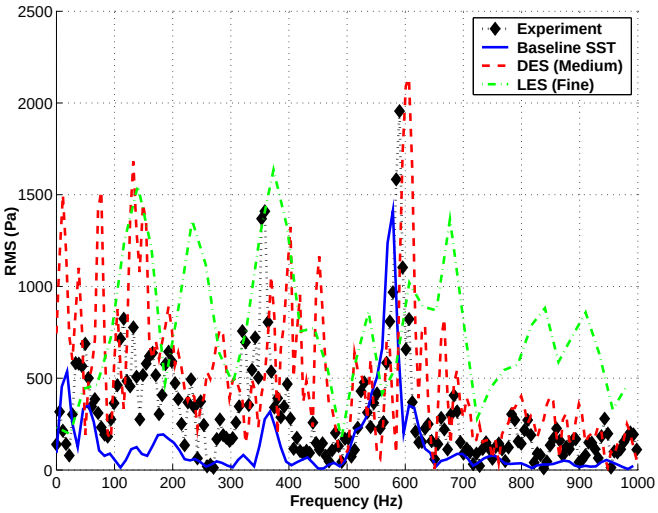

(b) PSD Plots (x/L=0.95)

Figure 5: SPL and PSD plots for L/D=5, W/D=1, clean cavity with no doors with URANS (Baseline SST turbulence model), DES (one-equation Spalart-Allmaras model) and LES (Smagorinsky SGS). The fine grid with a CFD time-step of 0.001 ($\equiv 1.814 \times 10^{-6}$s) was used for the LES calculation, the medium grid with a CFD time-step of 0.005 ($\equiv 9.07 \times 10^{-6}$s) for the DES computation and the coarse grid with a CFD time-step of 0.01 ($\equiv 1.814 \times 10^{-5}$s) for the URANS case. Both plots taken along cavity centreline (z/W=0.5) and at the cavity floor (y/D=1). See Figure 1 for reference to positions of pressure taps and Table 1 for details of the grids employed.

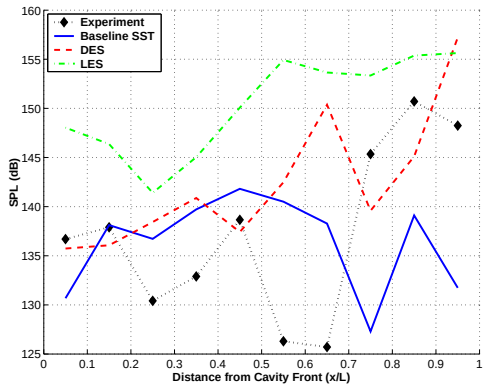

(a) 1st Rossiter Mode ($\approx$ 160 Hz)

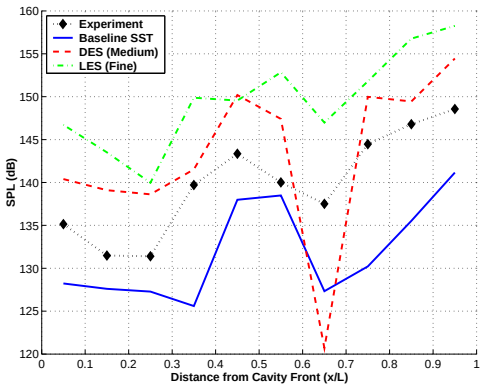

(b) 2nd Rossiter Mode ($\approx$ 380 Hz)

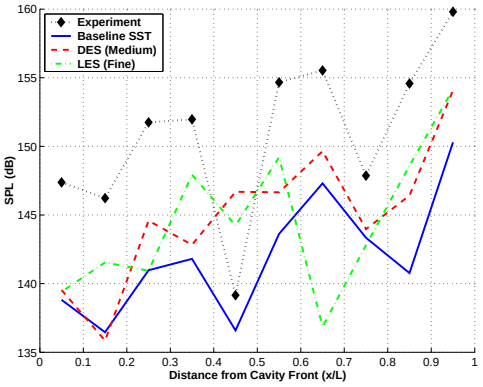

(c) 3rd Rossiter Mode ($\approx$ 600 Hz)

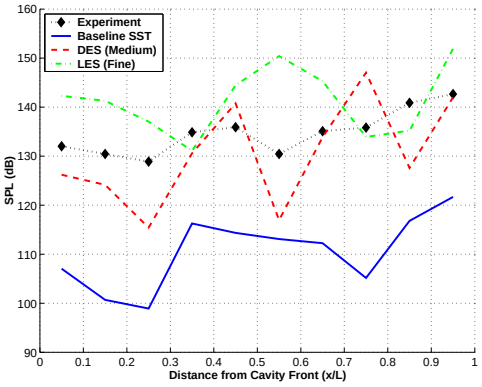

(d) 4th Rossiter Mode ($\approx$ 820 Hz)

Figure 6: Windowed SPL plots for the L/D=5, W/D=1, clean cavity with no doors with URANS (Baseline SST turbulence model), DES (one-equation Spalart-Allmaras model) and LES (Smagorinsky SGS) compared with experiment for the first 4 Rossiter modes. The fine grid with a CFD time-step of 0.001 ($\equiv 1.814 \times 10^{-6}$s) was used for the LES calculation, the medium grid with a CFD time-step of 0.005 ($\equiv 9.07 \times 10^{-6}$s) for the DES computation and the coarse grid with a CFD time-step of 0.01 ($\equiv 1.814 \times 10^{-5}$s) for the URANS case. Plots were taken along cavity centreline (z/W=0.5) and at the cavity floor (y/D=1). See Figure 1 for reference to positions of pressure taps and Table 1 for details of the grids employed.

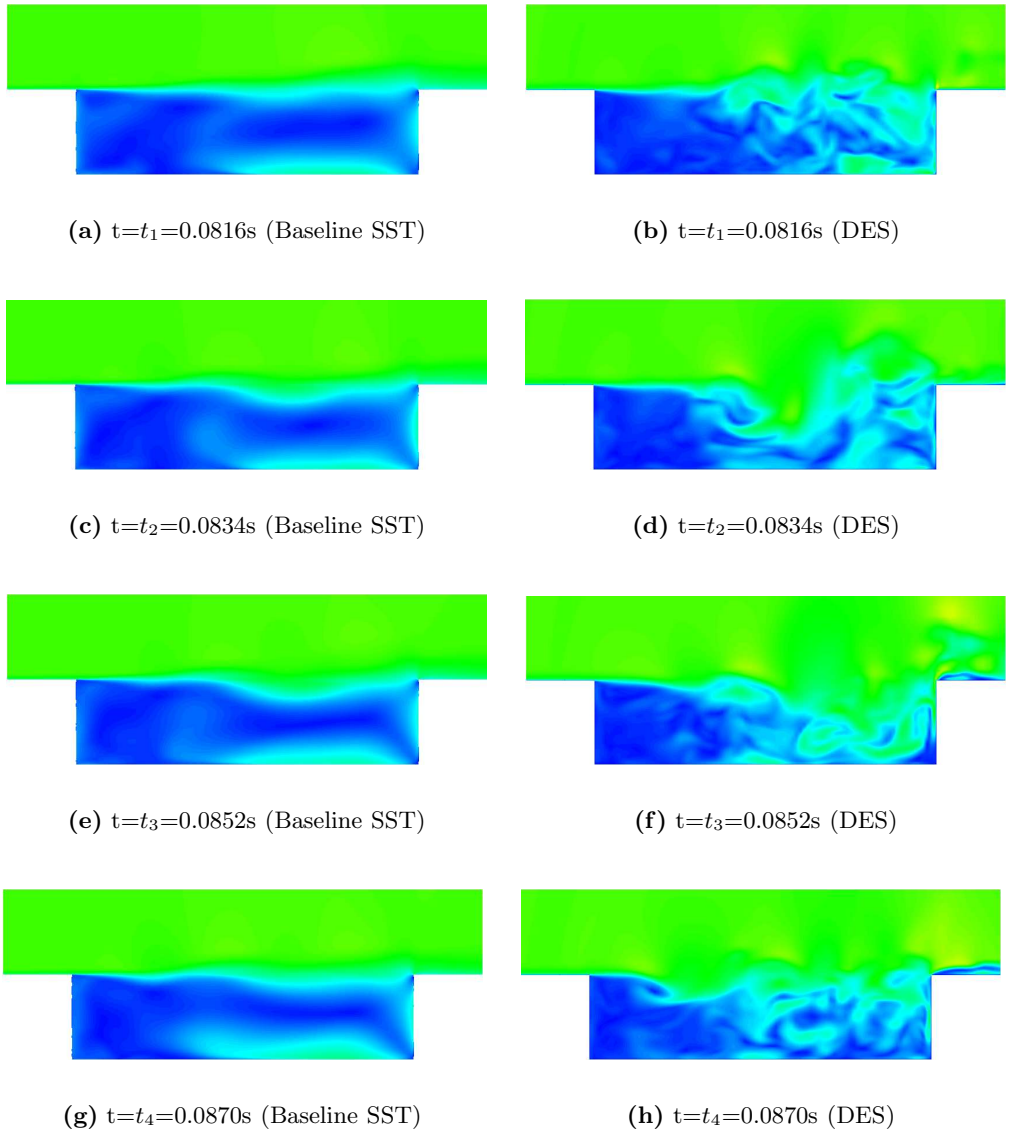

(a) t=t_1=0.0816s (Baseline SST)

(b) t=t_1=0.0816s (DES)

(c) t=t_2=0.0834s (Baseline SST)

(d) t=t_2=0.0834s (DES)

(e) t=t_3=0.0852s (Baseline SST)

(f) t=t_3=0.0852s (DES)

(g) t=t_4=0.0870s (Baseline SST)

(h) t=t_4=0.0870s (DES)

Figure 7: Instantaneous Mach contours with streamlines for the clean cavity with no-doors illustrating the flow features inside the 3D cavity at for 4 different time-steps during flow cycle for the URANS (Baseline SST turbulence model) and DES (one-equation Spalart-Allmaras turbulence model) computations. Plots taken along the cavity centreline (z/W = 0.5). See Figure 1 for reference to positions of pressure taps.

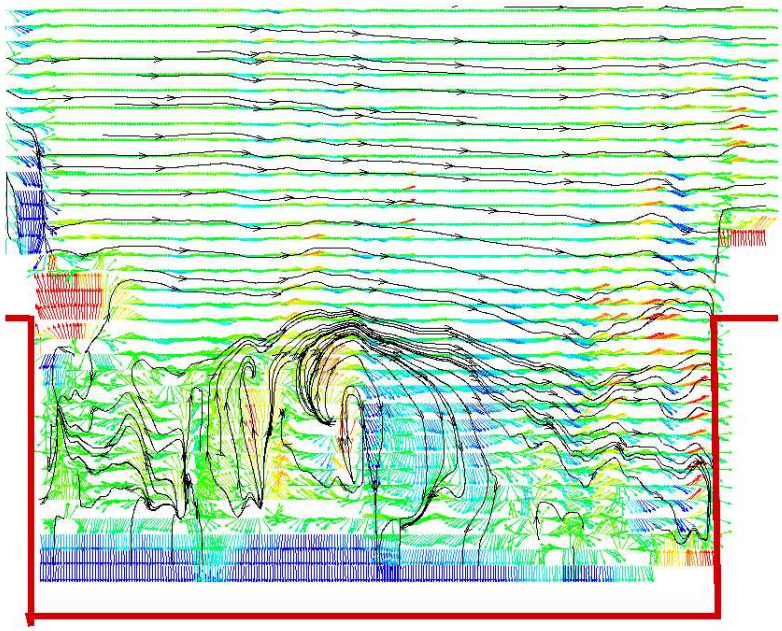

Figure 8: Instantaneous velocity magnitude contours with streamlines for the clean cavity with no-doors illustrating the flow features inside the 3D cavity for the PIV experiment. Shear layer fails to remain coherent after about middle of cavity. Straamlines observed to 'dip' into cavity near the downstream edge indicating that energy is transferred into the cavity from the shear layer as part of the redistribution and mixing process. Shear layer break-down and redistribution of momentum observed in DES computations but not in URANS (refer to Figure 7).

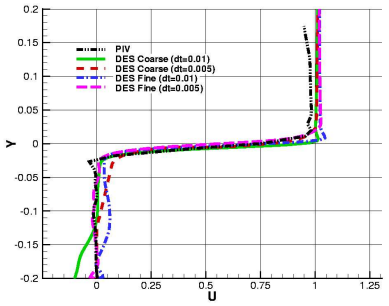

(a) U-Velocity (x/L=0.05)

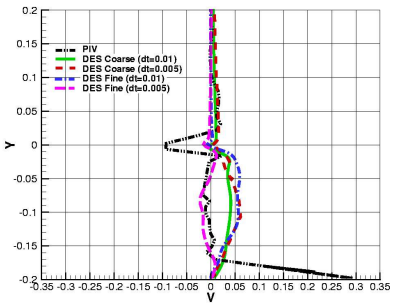

(b) V-Velocity (x/L=0.05)

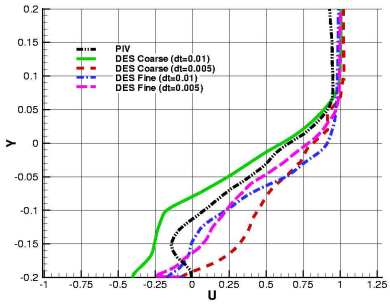

(c) U-Velocity (x/L=0.55)

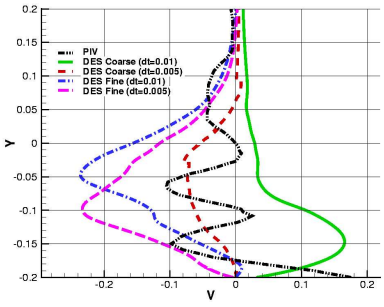

(d) V-Velocity (x/L=0.55)

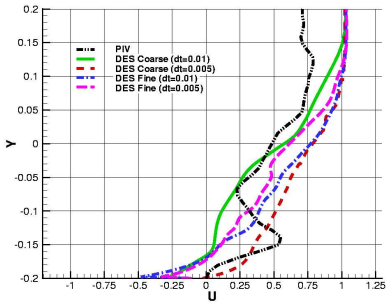

(e) U-Velocity (x/L=0.95)

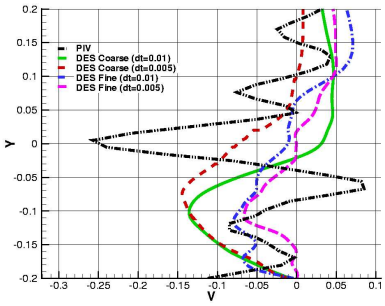

(f) V-Velocity (x/L=0.95)

Figure 9: Time-Averaged streamwise & transverse velocity profiles for the clean cavity with no-doors at 3 locations along cavity floor: cavity front (x/L=0.05), cavity middle (x/L=0.55) and cavity rear (x/L=0.95) for DES computations with coarse and medium grids for CFD time-steps of 0.01 ($\equiv 1.814 \times 10^{-5}$s) and 0.005 ($\equiv 9.07 \times 10^{-6}$s). Black Line corresponds to experimental PIV data (provided by Ross[4]). Plot Taken along cavity centerline (z/W=0.5). See Figure 1 for reference to positions of pressure taps and Table 1 for details of the grids employed.

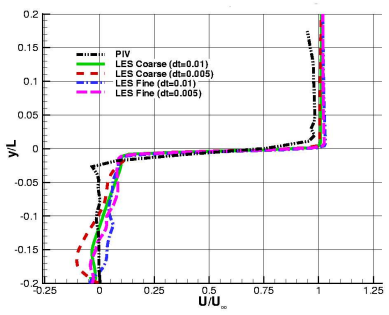

(a) U-Velocity (x/L=0.05)

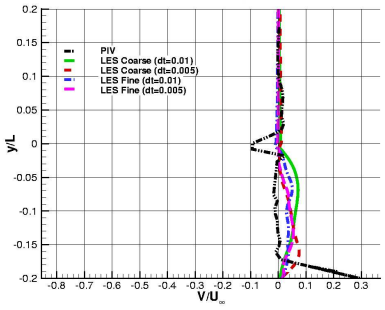

(b) V-Velocity (x/L=0.05)

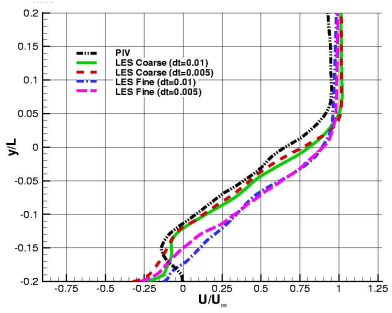

(c) U-Velocity (x/L=0.55)

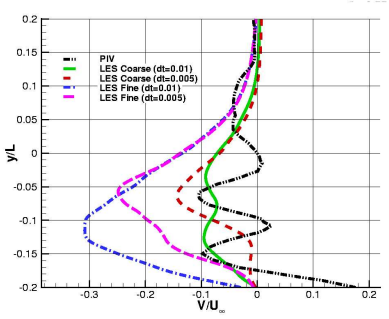

(d) V-Velocity (x/L=0.55)

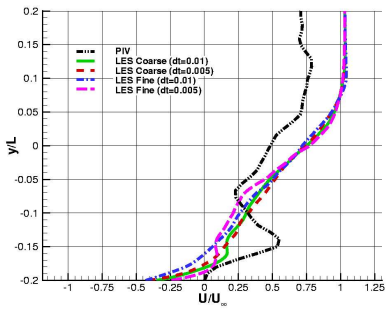

(e) U-Velocity (x/L=0.95)

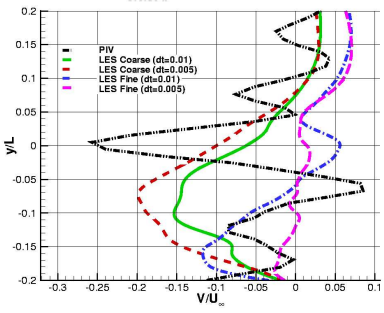

(f) V-Velocity (x/L=0.95)

Figure 10: Time-Averaged streamwise & transverse velocity profiles for the clean cavity with no-doors at 3 locations along cavity floor: cavity front (x/L=0.05), cavity middle (x/L=0.55) and cavity rear (x/L=0.95) for LES computations using the coarse and medium grids for CFD time-steps of 0.01 ($\equiv 1.814 \times 10^{-5}$s) and 0.005 ($\equiv 9.07 \times 10^{-6}$s). Black Line corresponds to experimental PIV data (provided by Ross[4]). Plot Taken along cavity centerline (z/W=0.5). See Figure 1 for reference to positions of pressure taps and Table 1 for details of the grids employed.

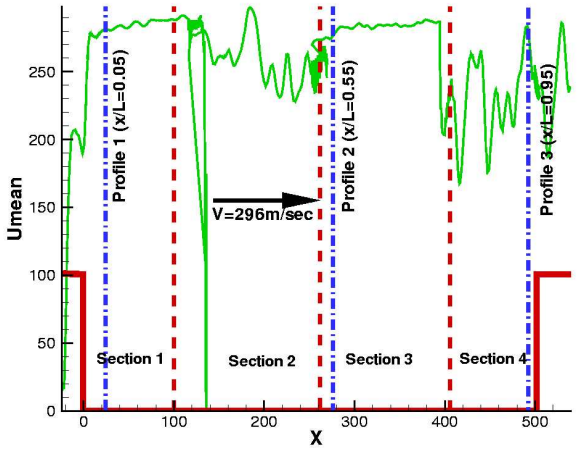

(a) PIV Streamwise (U) Velocity

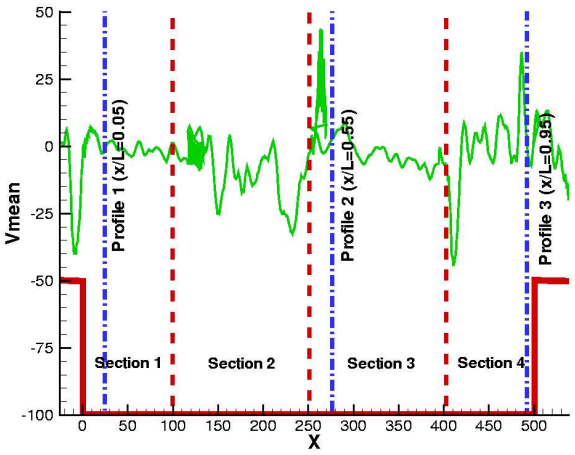

(b) PIV Transverse (V) Velocity

Figure 11: Streamwise & transverse velocity traces at a distance equal to the depth of the cavity above the cavity lip. PIV was performed at free-stream velocity of 296 m/s. At cavity front and around cavity middle the PIV resolution is good and the free-stream velocity calculated is as it should be. Near cavity rear PIV reslution is very poor and U-velocity is not 296m/s and fluctuates severely - transverse velocity plot indicates the same. As a result, comparisons with CFD poorest when comparing with PIV data at cavity rear (e.g. at x/L=0.95).